

Research Article

A Novel Method for Extracting Maximum Kurtosis Component and Its Applications in Rolling Bearing Fault Diagnosis

Yonggang Xu,^{1,2} Zeyu Fan,¹ Kun Zhang ,¹ and Chaoyong Ma¹

¹Key Laboratory of Advanced Manufacturing Technology, Beijing University of Technology, Chaoyang District, Beijing 100124, China

²Beijing Engineering Research Center of Precision Measurement Technology and Instruments, Beijing University of Technology, Beijing 100124, China

Correspondence should be addressed to Kun Zhang; zkun212@163.com

Received 26 March 2019; Revised 9 July 2019; Accepted 16 July 2019; Published 25 August 2019

Academic Editor: Adam Glowacz

Copyright © 2019 Yonggang Xu et al. This is an open access article distributed under the Creative Commons Attribution License, which permits unrestricted use, distribution, and reproduction in any medium, provided the original work is properly cited.

Rolling bearing plays an important role in the overall operation of the mechanical system; therefore, it is necessary to monitor and diagnose the bearings. Kurtosis is an important index to measure impulses. Fast Kurtogram method can be applied to the fault diagnosis of rolling bearings by extracting maximum kurtosis component. However, the final result may disperse the effective fault information to different frequency bands or find wrong frequency band, resulting in inaccurate frequency band selection or misdiagnosis. In order to find the maximum component of kurtosis accurately, an algorithm of frequency band multidivisional and overlapped based on EWT (MDO-EWT) is proposed in this paper. This algorithm changes the traditional Fast Kurtogram frequency bands division method and filtering method. It builds the EWT boundaries based on the maximum kurtosis component in each iteration and finally obtains the maximum kurtosis component. Through the simulation signal and the rolling bearing inner and outer ring fault signals verification, it is proved that the proposed method has a good performance on accuracy and effectiveness.

1. Introduction

Modern mechanical equipment tends to be universal, and rolling bearing is one of the important parts of rotating machinery. Bearing damage will further lead to equipment failure or even greater danger. Therefore, it is necessary to conduct real-time monitoring and fault diagnosis of bearing operation state [1]. When the bearing is damaged, due to its periodic operation, periodic shock will appear in the signals collected by the acceleration sensor. It is a basic way of modern fault diagnosis to collect and process the signals of the corresponding parts of the bearing and extract the components that may contain fault information in the signals [2].

Periodic shocks can be reflected by the kurtosis value. In 1983, Dwyer [3] proposed the statistical concept of spectral kurtosis (SK) and used it as a supplement to the power spectral density to extract the transient components of signals. Capdevielle et al. [4] gave a more formal definition based on the theory of higher-order statistics, but this

definition cannot effectively obtain the characteristic components of nonstationary signals. In recent years, some scholars have conducted in-depth research. An algorithm combining autoregressive linear predictive filtering and minimum entropy deconvolution (MED) was proposed to improve the monitoring and diagnosis ability of SK [5]. On this basis, combined with PPCA and spectral kurtosis, noise and low-frequency interference are effectively suppressed [6]. The spectral kurtosis-based fault extraction method is also widely used in various fields such as noise detection [7, 8]. The above literatures expand the application range of spectral kurtosis, but few of them are optimized. To identify adaptively resonance frequency band, Antoni creatively put forward the spectral kurtosis theory [9, 10] and rapid kurtosis figure (fast kurtogram) method [11], the proposed method since 10 years obtained the full affirmation and attention [12]. Antoni obtained the boundary by dividing the spectrum at equal intervals. The method of constructing the filter broadened the application range of the algorithm and simplified the solving logic, making great contributions to

the theoretical research and application of spectral kurtosis. However, the method also has its disadvantages: the method of splitting the spectrum results in the desired center frequency and side frequency band width, which cannot be reasonably explained theoretically. In the process of application, many scholars have put forward many excellent improvement schemes to improve the original diagnostic ability. In [13–15], respectively, Db wavelet, lifting multi-wavelet, and harmonic wavelet were applied to replace Antoni's STFT and semianalytical finite impulse response (FIR) filter banks, so as to improve the decomposition effect and extract fault features similar to wavelet basis function from the noise signal to the greatest extent. Li et al. [16] further proposed a multiscale band fusion method based on it. Dai et al. [17] proposed an improved method of spectral kurtosis averaging. Zhang et al. [18] used correlation kurtosis instead of kurtosis to identify resonance band in diagnosis from the consideration of periodicity of fault impact. To a certain extent, the traditional methods have been optimized and improved, and the diagnostic ability has been enhanced. However, fundamentally speaking, there are too many human factors involved in the boundary division in the frequency domain, and it is possible to find the maximum kurtosis by dividing the spectrum into different components, which may lead to the error of finding the maximum kurtosis frequency band. Moreover, the traditional frequency band division method may disperse the corresponding maximum frequency band of kurtosis to different frequency bands, resulting in information omission and affecting the final diagnosis result. Therefore, it is necessary to explore a method for extracting fault information by adaptive frequency division and signal reconstruction based on kurtosis index.

Empirical wavelet transform (EWT) is a fast developing fault extraction method in recent years. EWT is used to construct the filter and reconstruct its components in this article. In recent years, many scholars have studied and optimized the empirical wavelet transform. Gilles [19] put forward the empirical wavelet transform (EWT) on the basis of the adaptive and rigorous mathematical deduction process. Kedadouche et al. [20] verify that EWT can obtain better effect than EMD in extracting fault features and related harmonics associated with harmonics. Gilles and Heal then changed the Fourier spectrum into a function in the representation of scale space [21]. A new fast empirical wavelet transform method AFEWT is proposed in [22], which enhances the adaptability of EWT and optimizes the boundary problem. However, in the existing EWT methods, there are still problems of excessive components and how to establish boundaries.

To obtain the maximum kurtosis component, a new algorithm of frequency band multidivisional and overlapped based on EWT (MDO-EWT) is proposed in this paper. The method is to establish the boundaries of EWT filter according to the maximum kurtosis component in each iteration, and the final maximum kurtosis component can be obtained to extract the fault information. It improves the problems of fast kurtogram in frequency domain boundary division, such as rigid division, and it is easy to be affected by

noise. Compared to the FK method, the results showed the proposed method is more effective and accurate. The contents followed are organized as follows: Section 2 briefly introduces fast kurtogram and points out its shortcomings; in Section 3, the procedure of the proposed method and its core algorithm (MDO-EWT) are described in details and then EWT is introduced; the proposed method is analysed by two simulated signals in Section 4, and then preliminary verification by the diagnosis of rolling bearing inner and outer rings data is conducted in Section 5; in addition, further verification based on the experimental data of CWRU is given in Section 6; finally, the conclusion is drawn in Section 7.

2. Theoretical Background

2.1. Basic Theory and Techniques for Fast Kurtogram. For nonstationary processes, the calculation of spectral kurtosis depends on the selection of frequency resolution. Spectral kurtosis can be regarded as a function $(f, \Delta f)$ of frequency and frequency resolution. Therefore, the calculation of spectral kurtosis is transformed into the problem of how to select the frequency resolution on a known frequency range. For the convenience of expression, spectral kurtosis on the plane of $(f, \Delta f)$ is represented by the kurtosis diagram, and the specific steps can be summarized as follows:

- (1) *Filtering.* The core of fast kurtogram is to construct a tree-like band-pass filter bank. There are two traditional filtering methods, one is based on the short-time Fourier transform (STFT), using the frequency-band dichotomy decomposition method. The other is a finite impulse response filter (FIR), using the frequency band alternating dichotomy and tripartite method. The frequency band is divided into low frequency and high frequency by the dichotomy method, and low frequency, middle band pass, and high frequency by the tripartite method. The original signal spectrum is used as the initial dividing source, and the divided frequency band can also be used as the dividing source alternately into two or three parts. In this way, a frequency band division tower-fast spectral kurtosis graph can be obtained. Figure 1 shows the 1/3-binary tree filter bank schematic diagram based on FIR filtering.
- (2) *Reconstruct the components and calculate kurtosis.* After the reconstruction of the segmented frequency bands, the kurtosis values of the components are obtained, and the kurtosis values of different sizes are defined into different colors by filling them into Figure 1 to form the kurtosis diagram.
- (3) Obtain the corresponding component of the maximum kurtosis and conduct envelope demodulation for fault diagnosis.

2.2. Drawbacks of the FK Method. In order to elaborate the deficiency of the FK method, the following simulated signal with equal intervals and noise are constructed. It is defined

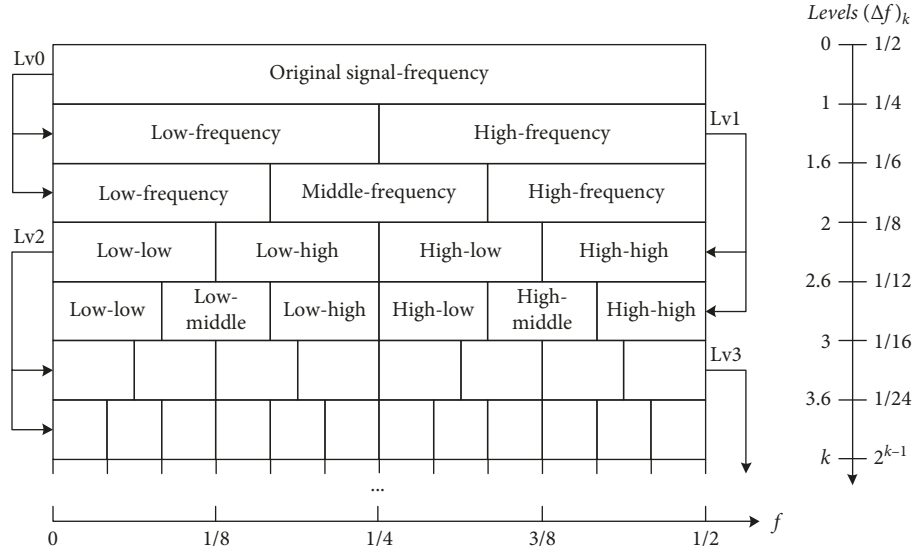


FIGURE 1: Frequency-band division using the 1/3-binary tree filter bank.

as the following equation, and the parameters of the simulated signal are shown in Table 1:

$$\begin{cases} s_1 = 6e^{-g \times 2\pi f_0 t} \times \sin(2\pi f_0 t \times \sqrt{1-g^2}), \\ s = s_1 + \eta. \end{cases} \quad (1)$$

Suppose the sampling frequency is 12000 Hz, and take $N = 12000$ points for analysis. Figures 2(a) and 2(c) are kurtosis graphs obtained by using FIR and STFT modes in the FK method, respectively. Figures 2(b) and 2(d) show the spectrum of the signal and the division method. The red dotted line is the approximate correct frequency band range, while the black dotted line corresponds to the frequency band range obtained by the FK method. It can be found when FK divides the boundary in frequency domain, there are many human factors, as it can only be divided into fixed equal parts. There is no theoretical support for selecting the maximum kurtosis component from the divided frequency bands, and it is impossible to prove the central frequency and the side band width. The problems that result from this approach are summarized as follows:

- (1) The maximum kurtosis component is just noise, and no effective information can be obtained (Figures 2(a) and 2(b)).
- (2) The maximum kurtosis component can be found inaccurately. The corresponding frequency band is too narrow, leading to the dispersion of the real frequency band into different frequency bands (Figures 2(c) and 2(d)).

3. The Proposed Method for Bearing Fault Diagnosis

In view of the above shortcomings of FK, the article proposes an algorithm of frequency band multidivisional and overlapped by using EWT for filtering, which is more accurate and effective to obtain the maximum kurtosis component. The flowchart of the proposed method is shown in Figure 3. The specific steps are summarized as follows:

TABLE 1: Parameters of the simulation signal.

Natural frequency (s_1)	Damping factor	Fault characteristic frequency	Noise
$f_0 = 1500$ Hz	$g = 0.07$	100 Hz	SNR = -8 db

- (1) Define the original signal as $y(t)$ and use fast-Fourier transform algorithm (FFT) to get the spectrum $Y(f)$, then define the initial frequency band to be divided as $B = (0, \pi)$, and set the number of iteration $i = 1$.
- (2) Divide the frequency band into 6 segments uniformly and merge each segment with the next segment. At this time, the frequency band is divided into 5 overlapping segments.
- (3) Select Meyer wavelet as the basis function, and then use the corresponding scaling function and empirical wavelet to establish two sets of adaptive filter. We can get 5 segments and 5 reconstructed time-domain components after this.
- (4) Calculate kurtosis of all the reconstructed time-domain components, respectively. Then, the corresponding frequency band of the maximum kurtosis component and the frequency band overlapped with it are found. They are regarded as the new frequency band to be divided. At this time, $i = i + 1$, and if $i \leq 5$, steps (2) to (4) are repeated.
- (5) According to the cyclic cutoff condition, the envelope spectrum is obtained for the finally found maximum kurtosis component, and corresponding fault information is extracted.

3.1. The Algorithm of Frequency Band Multidivisional and Overlapped Based on EWT. When $i = 1$, the frequency band to be divided is defined as $B = (0, \pi)$. The division of the spectrum and the bandpass range of the filters based on

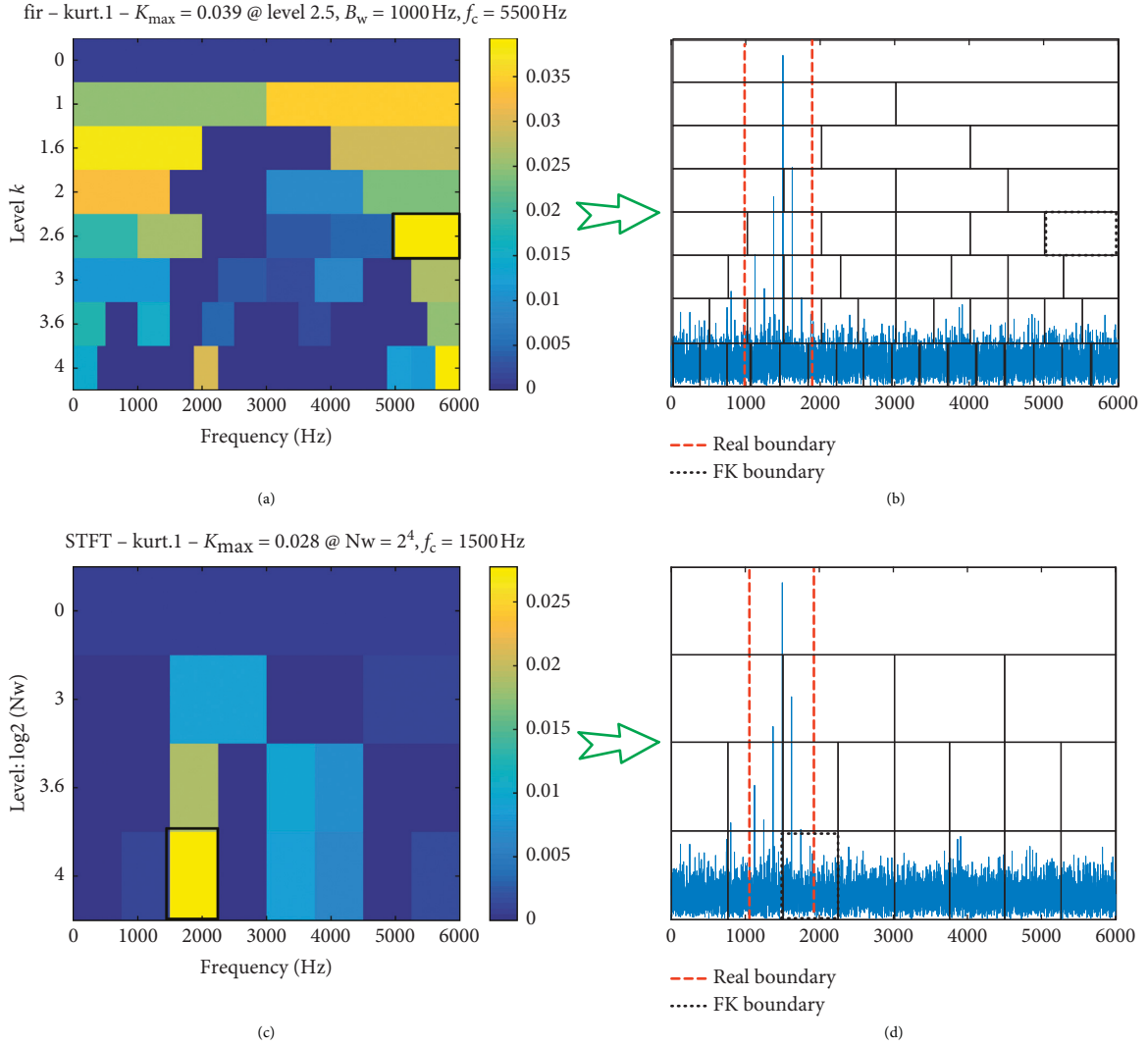


FIGURE 2: (a) Results by the FIR filter; (b) spectrum and the division method of FIR mode; (c) results by the STFT filter; (d) spectrum and the division method of the STFT mode.

EWT are shown in Figure 4. In Figure 4(a), the subscript W represents the frequency band start-stop label, and the upper subscript indicates the number of iteration. The letters A_1-E_1 , respectively, represent the five overlapped bands, and at this iteration, $w_0^1 = 0$, $w_6^1 = \pi$. Figure 4(b) is a schematic diagram of two sets of filters. The result is that the divided frequency bands A_1-E_1 are filtered out.

When $i \geq 2$, the frequency band to be divided needs to be reselected. The schematic diagram of choosing the new frequency band is shown in Figure 5. The frequency band C_1 corresponding to the maximum kurtosis component can be obtained from the kurtosis value polyline graph in Figure 5(a). It can be inferred that most of the maximum kurtosis component's frequency band range is in band C_1 , but a small part may exist in adjacent frequency bands. In order to ensure the integrity of the maximum kurtosis component, frequency band C_1 and all overlapped frequency bands B_1 and frequency band D_1 are selected as a new frequency band to be divided. Figure 5(b) shows the divided frequency bands A_2-E_2 of the new frequency band

$B_1 + C_1 + D_1$. $W_0^2 = W_1^1$, $W_6^2 = W_4^1$ at this iteration. Figure 5(c) is a schematic diagram of two groups of filters based on the new boundary. Figure 5(d) indicates the new kurtosis polyline graph and the new frequency band to be divided after reconstructing components A_2-E_2 .

In each iteration, the frequency band corresponding to the maximum kurtosis component can be summarized into two categories. Category 1: frequency band B or frequency band C or frequency band D is the frequency band corresponding to the maximum kurtosis component, so the new frequency band to be divided is $A + B + C$, $B + C + D$, $C + D + E$, respectively. At this time, the bandwidth of the new band is $2/3$ of the last bandwidth. Category 2: frequency band A or frequency band E is the frequency band corresponding to the maximum kurtosis component, so the new frequency band to be divided is $A + B$, $D + E$, respectively. At this time, the bandwidth of the new band is $1/2$ of the last bandwidth. Therefore, the final bandwidth obtained by the filter is $(1/2)^{i-1} \sim (2/3)^{i-1}$ of the original signal frequency bandwidth $([0, \pi])$. In general, the sampling frequency is above 5000 Hz,

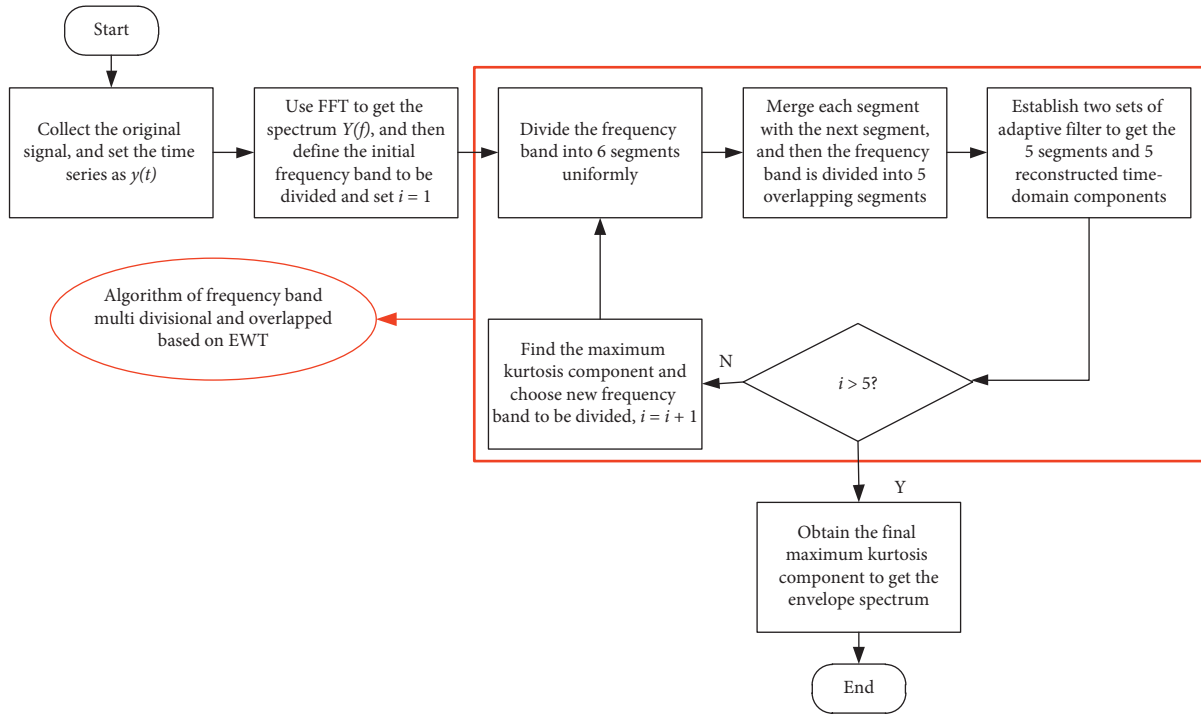


FIGURE 3: The flowchart of the proposed method.

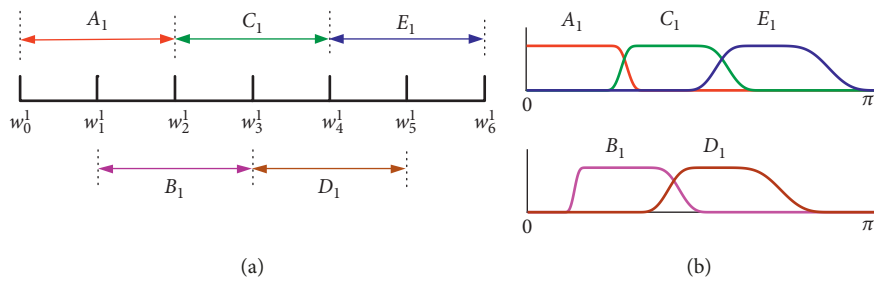


FIGURE 4: (a)The division of the spectrum when $i = 1$; (b) two sets of EWT-based filters when $i = 1$.

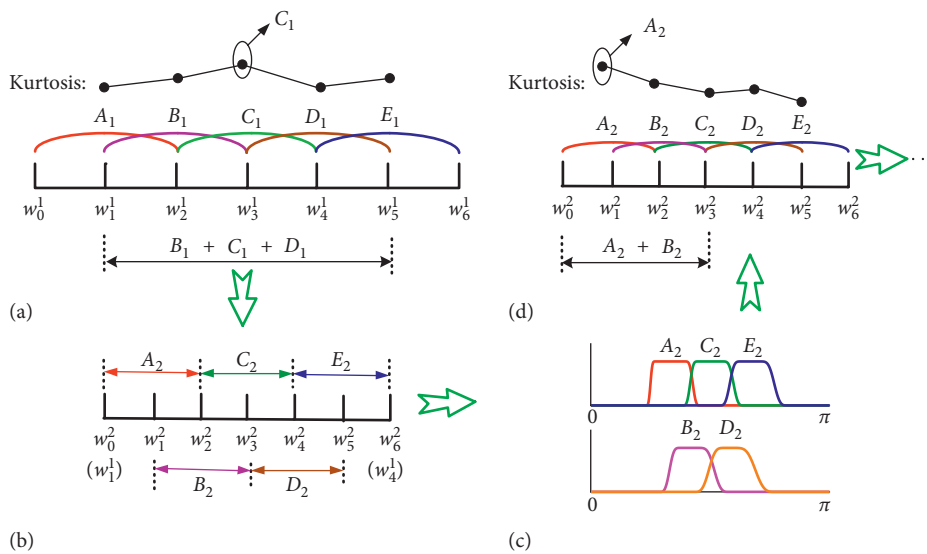


FIGURE 5: (a)Kurtosis polyline graph and new frequency band to be divided; (b) the division of the spectrum when $i = 2$; (c) two sets of EWT-based filters when $i = 2$; (d)kurtosis polyline graph and new frequency band to be divided in the next iteration.

and the fault extraction in the envelope spectrum needs to find the characteristic frequency and its 2~3 frequency doubling. Considering the above considerations and according to many times experiences, the spectrum could be divided into mutually overlapped five segments each time, and the number of loops could be set as 5.

3.2. Basic Theory for EWT. The empirical wavelet transform is actually the adaptive division of the Fourier spectrum and the establishment of a set of wavelet filters suitable for the signal to be processed. The empirical wavelet transform method can be simply described in the following three steps:

Step 1: Defining Boundaries. The spectrum range is defined as $[0, \pi]$. Assuming that the signal spectrum is divided into N continuous intervals, it is necessary to determine $N+1$ boundary lines, where 0 and π

are the first and last boundary lines, respectively, ($\omega_0 = 0, \omega_N = \pi$). In addition, it is also necessary to determine the other $N-1$ boundary lines ($\omega_1, \omega_2, \dots, \omega_{N-1}$). Then, each frequency band can be as follows: $\Lambda_n = [\omega_{n-1}, \omega_n]$, $n = 1, 2, \dots, N$. Obviously, $\cup_{n=1}^N \Lambda_n = [0, \pi]$. Choose ω_n as the centre frequency, and then define a transition section of $T_n = 2\tau_n$ width to construct the window base. In this paper, the boundaries are established by the proposed method.

Step 2: Filter Out Frequency Band $\Lambda_n = [\omega_{n-1}, \omega_n]$, $n = 1, 2, \dots, N$, *Respectively.* Gilles constructed empirical wavelets based on the Meyer wavelet construction method [19]. A set of mutually orthogonal trigonometric functions are designed in the transition section. Therefore, the empirical scale function $\widehat{\mathcal{O}}_n(\omega)$ and the empirical wavelet function $\widehat{\Psi}_n(\omega)$ are defined as follows:

$$\widehat{\mathcal{O}}_n(\omega) = \begin{cases} 1; & |\omega| \leq (1-\gamma)\omega_n, \\ \cos\left[\frac{\pi}{2}\beta\left(\frac{1}{2\gamma\omega_n}(|\omega| - (1-\gamma)\omega_n)\right)\right]; & (1-\gamma)\omega_n \leq |\omega| \leq (1+\gamma)\omega_n, \\ 0; & \text{others,} \end{cases}$$

$$\widehat{\Psi}_n(\omega) = \begin{cases} 1; & (1+\gamma)\omega_{n+1} \leq |\omega| \leq (1-\gamma)\omega_{n+1}, \\ \cos\left[\frac{\pi}{2}\beta\left(\frac{1}{2\gamma\omega_{n+1}}(|\omega| - (1-\gamma)\omega_{n+1})\right)\right]; & (1-\gamma)\omega_{n+1} \leq |\omega| \leq (1+\gamma)\omega_n, \\ \sin\left[\frac{\pi}{2}\beta\left(\frac{1}{2\gamma\omega_n}(|\omega| - (1-\gamma)\omega_n)\right)\right]; & (1-\gamma)\omega_n \leq |\omega| \leq (1+\gamma)\omega_n, \\ 0; & \text{others.} \end{cases} \quad (2)$$

And, the transition function $\beta(x)$, the coefficient γ , and the transition phase τ_n are as follows:

$$\beta(x) = x^4(35 - 84x + 70x^2 - 20x^3),$$

$$\gamma < \min\left(\frac{\omega_{n+1} - \omega_n}{\omega_{n+1} + \omega_n}\right), \quad (3)$$

$$\tau_n = \gamma\omega_n, \quad 0 < \gamma < 1.$$

Step 3: Reconstructing Components. Define empirical wavelet transform as W_f^e , the Fourier transform as $F(\cdot)$, and the inverse Fourier transform as $F^{-1}(\cdot)$:

$$W_f^e(n, t) = \langle f(t), \psi_n(t) \rangle = \int f(\tau) \overline{\psi_n(\tau - t)} d\tau$$

$$= F^{-1}\left(\widehat{f}(\omega) \overline{\widehat{\Psi}_n(\omega)}\right). \quad (4)$$

The approximate coefficients $W_f^e(0, t)$ are generated by the inner product of the signal and the empirical scaling function:

$$W_f^e(0, t) = \langle f(t), \mathcal{O}_1(t) \rangle = \int f(\tau) \overline{\mathcal{O}_1(\tau - t)} d\tau$$

$$= F^{-1}\left(\widehat{f}(\omega) \overline{\widehat{\mathcal{O}}_1(\omega)}\right). \quad (5)$$

$\widehat{x}(\omega)$, $\widehat{\psi}_n(\omega)$, and $\widehat{\mathcal{O}}_1(\omega)$, respectively, represent the Fourier transform of x , $\psi_n(\omega)$, and $\mathcal{O}_1(\omega)$, and then the signal can be reconstructed as follows:

$$f(t) = W_f^e(0, t) * \mathcal{O}_1(\omega) + \sum_{n=1}^N W_f^e(n, t) * \psi_n(t)$$

$$= F^{-1}\left(\widehat{W}_f^e(0, \omega) \widehat{\mathcal{O}}_1(\omega) + \sum_{n=1}^N \widehat{W}_f^e(n, \omega) \widehat{\psi}_n(\omega)\right). \quad (6)$$

TABLE 2: Parameters of simulation signal in case study 1.

Natural frequency (s_1)	Damping factor	Fault characteristic frequency	Noise
$f_0 = 3000$ Hz	$g = 0.07$	100 Hz	SNR = -10 db

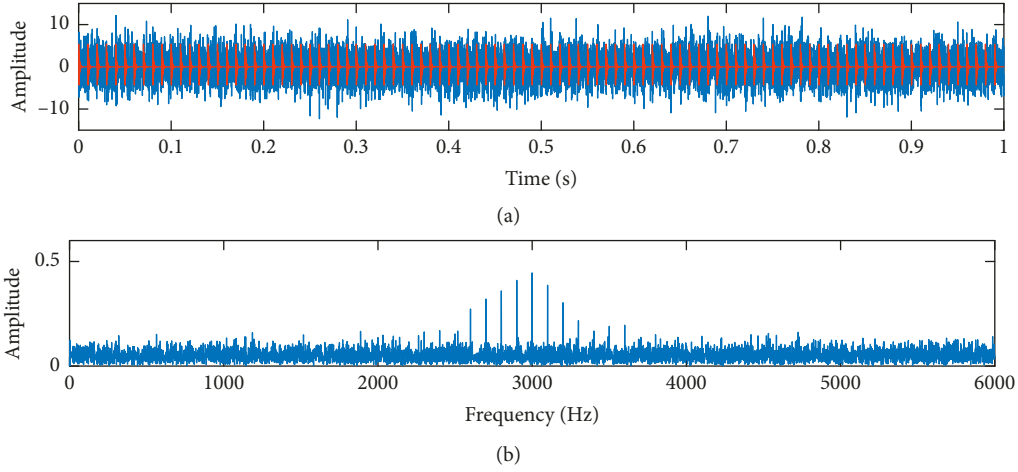


FIGURE 6: (a) Red: the impulsive signal; blue: the simulated signal mixed with impulsive signal and white Gaussian noise with SNR -10 dB; (b) the spectrum of the simulated signal.

$\widehat{W}_f^e(0, \omega)$ and $\widehat{W}_f^e(n, \omega)$, respectively, represent the Fourier transform of $W_f^e(0, t)$ and $W_f^e(n, t)$. The empirical mode is defined as follows:

$$\begin{cases} f_0(t) = W_f^e(0, t) * \varnothing_1(t), \\ f_k(t) = W_f^e(k, t) * \psi_k(t). \end{cases} \quad (7)$$

After obtaining the empirical mode of the signal, the Hilbert transform can be used to diagnose faults.

4. Simulated Signal Analysis

The FK method cannot correctly find the signal with center frequency as $f = 1/2^n \times F_S$, nor can it correctly find reasonable bandwidth. Two sets of simulation signals are given in this paper to prove that the proposed method is reasonable and effective in dividing the boundary.

4.1. Case Study 1. The equal-interval impulse signal s_1 changed the parameter f_0 in equation (1) to $f_0 = 3000$ Hz so as to prove that the new method could accurately find the frequency band with the center frequency of $f = 1/2 \times F_S$. And, we increased the η to SNR = -10 db. Suppose the sampling frequency is 12000 Hz, and take $N = 12000$ points for analysis. The specific parameters of the signal are shown in Table 2. Figure 6 shows the time domain diagram of the new s_1 and s and the spectrum of s .

The mode FIR is used to deal with the signal (s); Figure 7 shows the results; in Figure 7(a), the frequency band is searching for errors, and the component is extracted to make a time domain diagram to obtain the Hilbert transform. In the envelope diagram, there is no characteristic frequency, as shown in Figure 7(b). Figure 8 shows the results of fast kurtogram based on the mode STFT. In Figure 8(b) envelope

sequence, it can be seen that the characteristic frequency of 100 Hz and the frequency doubling of 200 Hz are found, but the amplitude of 3 frequency doubling is close to the noise, so it is not obvious. The result shows STFT found part of the real frequency band, but not accurately. Moreover, the left boundary is regarded as the centre frequency in the STFT mode, which is inconsistent with the reality.

Figure 9 shows the time domain waveform, spectrum, and envelope spectrum of the maximum kurtosis component obtained by using the proposed method. In Figure 9(a), sideband phenomenon can be seen clearly in its frequency band, and the starting frequency of 2605 Hz and stopping frequency of 3395 Hz can be obtained. The calculated central frequency is the same as $f_0 = 3000$ Hz. As it is shown in Figure 9(b), characteristic frequency 100 Hz and 2-6 frequency doubling are obviously found. In conclusion, effective information in the simulated signal has been successfully extracted.

4.2. Case Study 2. The collected engineering signals may contain similar nonimpulse but edge-frequency modulated signals in other frequency bands, which may cause interference. In the case study 2, a modulating signal s_2 that simulates other irrelevant information is added on the basis of equal-interval impulse signal. The equal-interval impulse signal changed the parameter f_0 in equation (1) to $f_0 = 2000$ Hz and increased the noise of η to SNR = -12 db. Suppose the sampling frequency is 12000 Hz, and take $N = 12000$ points for analysis. Signals s and s_2 are expressed as follows, and the specific parameters are shown in Table 3.

$$\begin{cases} s_2 = 2 \sin(100\pi \times t) \times \sin(2000\pi \times t + \sin(200\pi \times t)), \\ s = s_1 + s_2 + \eta. \end{cases} \quad (8)$$

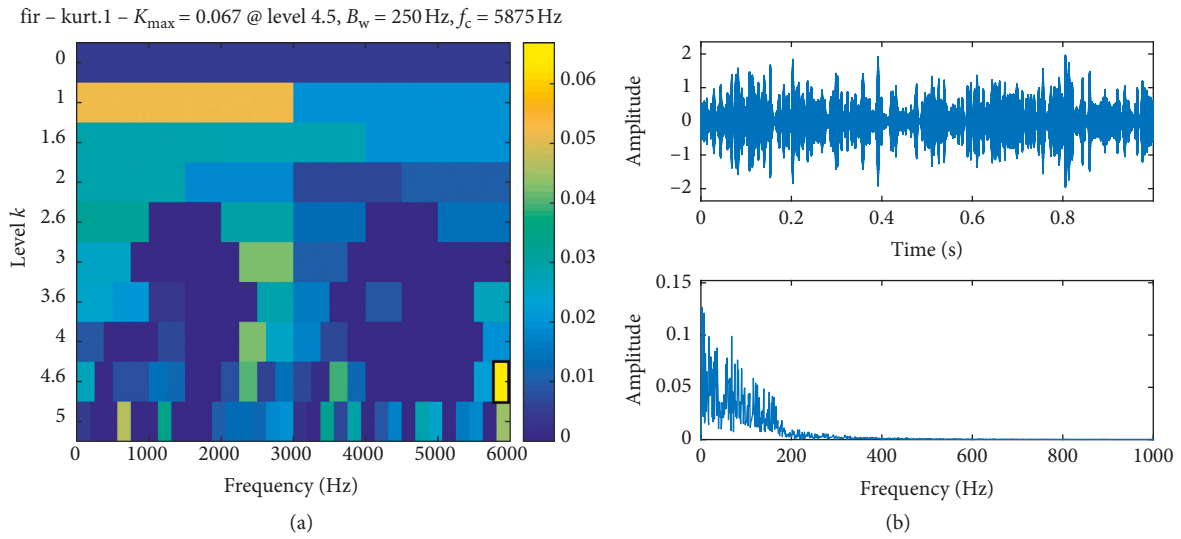


FIGURE 7: (a) Fast kurtogram based on FIR; (b) signal component and its envelope sequence.

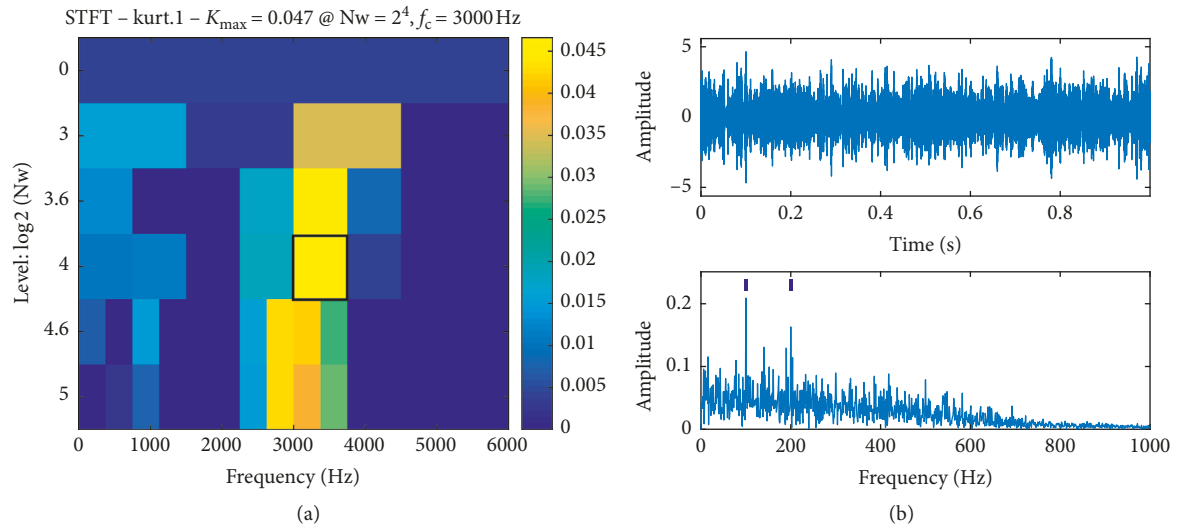


FIGURE 8: (a) Fast kurtogram based on STFT; (b) signal component and its envelope sequence.

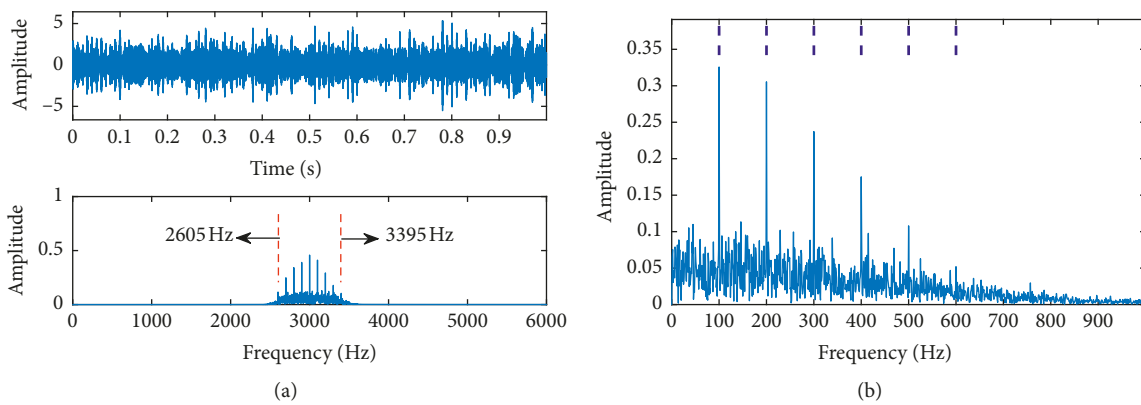


FIGURE 9: (a) Time-domain waveform diagram of the signal component with the maximum kurtosis found by the new method and its frequency band; (b) its envelope sequence.

TABLE 3: Parameters of the simulation signal in case study 2.

Natural frequency (s_1)	Signal components	Fault characteristic frequency	Noise
$f_0 = 2000$ Hz	s_1, s_2, η	100 Hz	SNR = -12 db

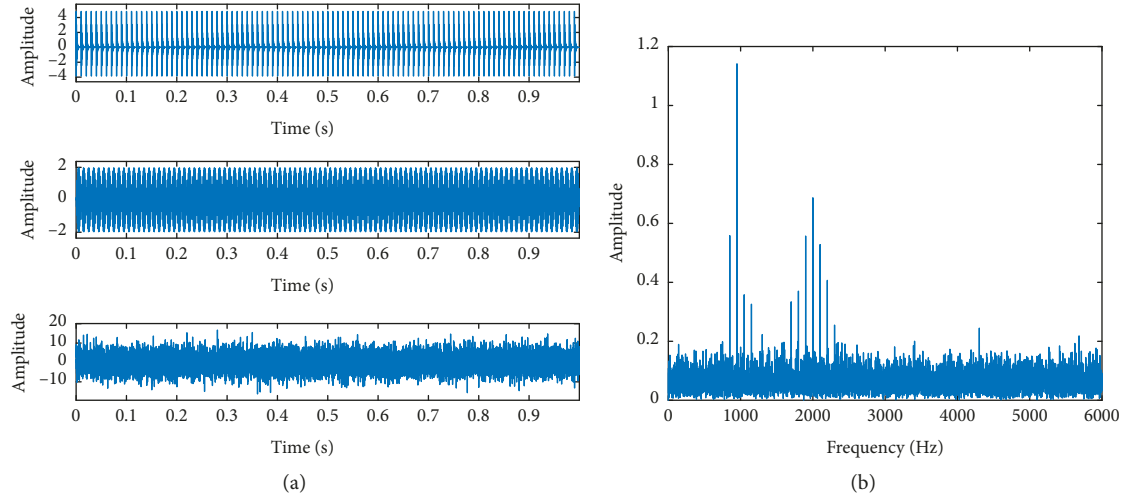


FIGURE 10: (a) The new impulsive signal s_1 ; (b) the modulation signal s_2 ; (c) the simulated signal s mixed with (a) and (b) and a white Gaussian noise with SNR -12 dB; (d) the spectrum of new simulated signal.

Figures 10(a)–10(c) show the time-domain diagrams of s_1, s_2 and s . Two resonance frequency bands are clearly found in Figure 10(d).

Figure 11 shows the results of processing the signal (s) by using the FK method, where (a) and (b) are using the FIR filter and (c) and (d) are based on STFT. It can be concluded from the figure that due to the influence of signal noise and modulation signal, neither of the two methods can find a reasonable frequency band and extract any useful information from the envelope spectrum.

Figure 12 shows the results obtained by the new method. According to Figure 12(a), the final frequency band range is (1604 Hz, 2396 Hz), bandwidth is $B_W = 790$ Hz, and center frequency is 2000 Hz, which fully conforms to the natural frequency $f_0 = 2000$ Hz of the medium interval impulse signal. As shown in Figure 12(b) envelope diagram, characteristic frequency 100 Hz and 2–5 frequency doubling are observed, which is highly diagnostic. This indicates that the proposed method is more reliable under more complex working conditions, such as increased noise and interference of other resonance components in the signal.

4.3. Quantitative Verification Based on Simulated Signal Energy Ratio. Simulated signals were used to verify the accuracy of the proposed method quantitatively from the point of signal energy. The original simulated signal can be described as the effective signal with noise, the effective signal energy accounts for the vast majority of the total energy, and the noise energy accounts for a small part. After the extracting process, the component obtained under ideal conditions should be all effective signals plus a small amount of noise; due to the presence of a small

amount of noise, the energy of the extracted signal must be higher than the pure effective signal energy. If the extracting component is less effective, the following two situations can occur:

- (1) Partly effective signal is extracted
- (2) Failing to extract the effective signal, and the extracted part is all noise

When the extracted signal energy in situation (1) is compared to the pure effective signal energy, due to the presence of noise, we cannot tell whose energy is higher. However, when compared with the extracted signal energy at ideal extraction conditions, the former signal energy must be lower than the latter, since the effective part in situation (1) is less and the effective signal accounts for the vast majority of the total energy. In situation (2), the extracted signal (noise) energy must be lower than the pure effective signal energy.

The discrete signal energy can be expressed by the sum of the squares of the discrete points. According to the SNR formula, the energy ratio (ER) is defined as follows:

$$\text{Energy Ratio} = \frac{E_1}{E_2} = \frac{\sum_{k=1}^N C_k^2}{\sum_{s=1}^N C_s^2}, \quad (9)$$

where C_k is the effective component extracted based on the kurtosis index and C_s is the pure effective fault signal (the equal-interval impulse signal s_1).

From the energy point of the simulated signal, we can conclude if the extraction effect is better, the energy ratio is higher; and ER must be < 1 in situation (2), $ER > 1$ in ideal situation, and $ER(\text{ideal situation}) > ER(\text{situation (2)})$.

The energy ratio histograms (Figure 13) of case 1 and case 2 by different methods are as follows.

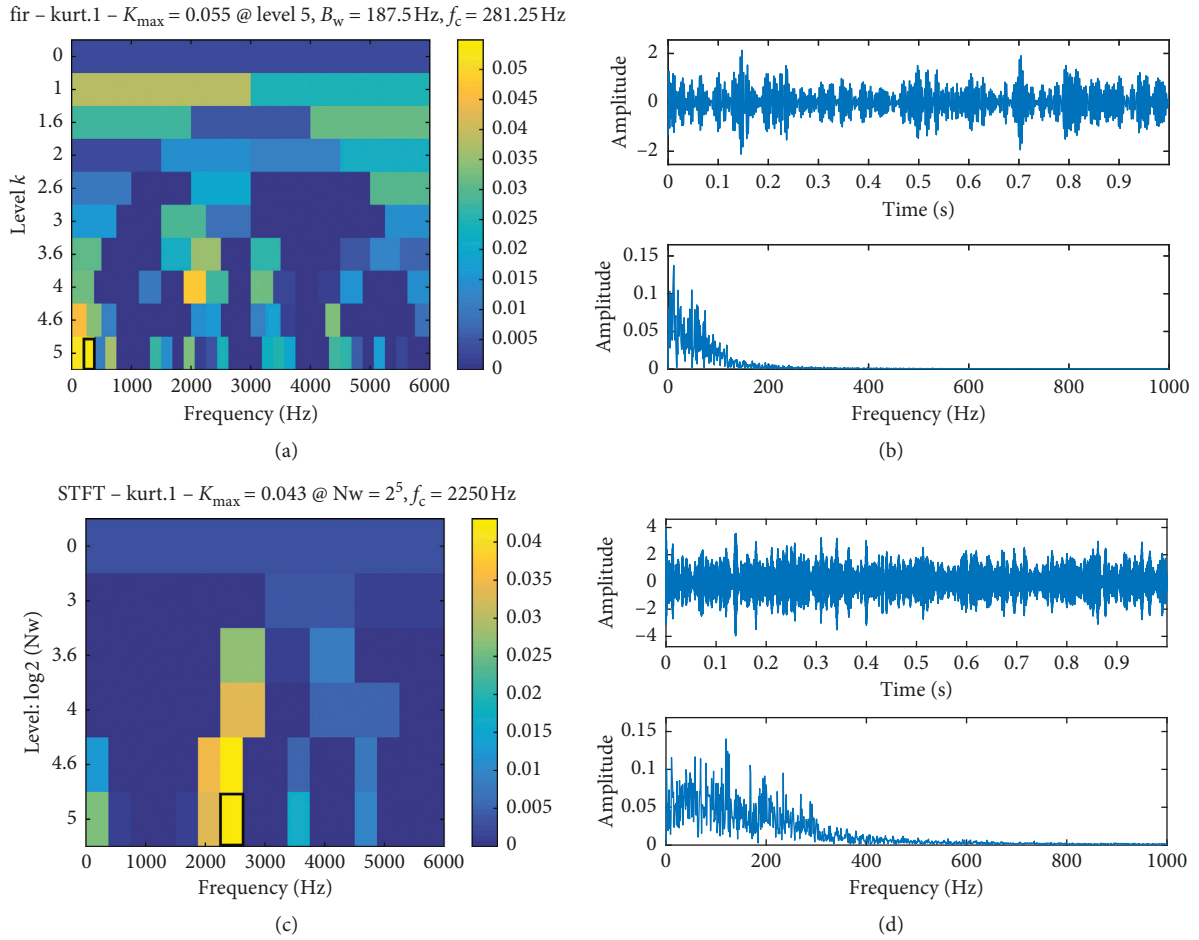


FIGURE 11: Fast kurtogram based on (a) FIR and (c) STFT; signal component and its envelope sequence by (b) FIR and (d) STFT.

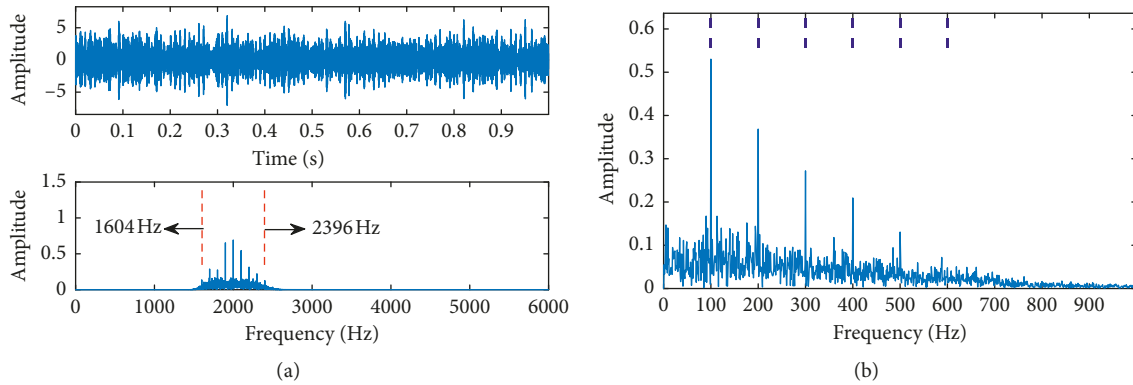


FIGURE 12: (a) Time-domain waveform diagram of the signal component with the maximum kurtosis found by the new method and its frequency band and (b) its envelope sequence.

In Figure 13(a), the energy ratio of case 1 processed by MOD-EWT is the largest and followed by FK-STFT, which is consistent with the number of characteristic frequencies in the envelope spectrum. In Figure 13(b), the signal energy ratio of case 2 processed by FK-FIR and FK-STFT methods is very small, which is consistent with the noise in envelope spectrum. This further illustrates the accuracy of the proposed method.

5. Analysis and Preliminary Verification by Two Experimental Signals

In this paper, two groups of experimental data were used to preliminarily verify the effectiveness of the proposed method. The first group was the bearing outer ring fault data, and the second group was the bearing inner ring fault data. The analysis and comparison with FK methods are given here in detail.

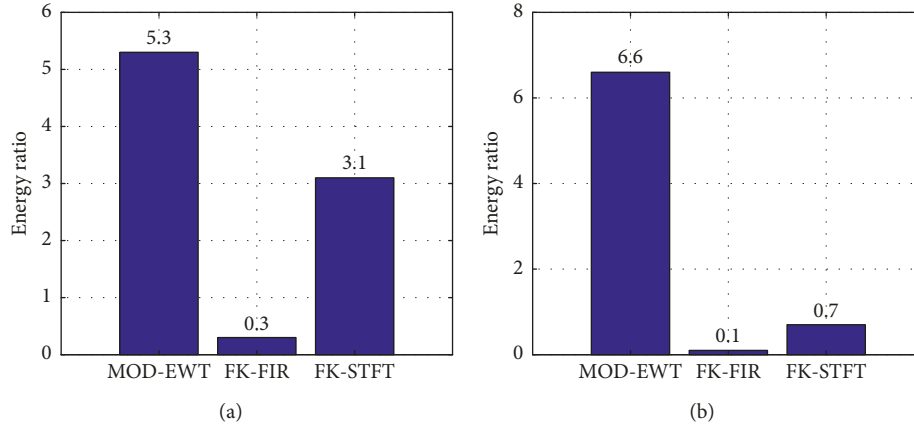


FIGURE 13: (a) Energy ratio histogram of case 1 by three methods; (b) energy ratio histogram of case 2 by three methods.

5.1. Analysis of Bearing Outer Ring Fault Data. In this part, the test data of faulty bearing from Xi'an Jiaotong university laboratory were used. Figure 14 is a schematic diagram of the test bed. The fault bearing number is ER-12K. The specific parameters are shown in Table 4. The sensor was connected to the outer ring of the bearing near the motor end. The actual motor frequency was 33.6 Hz, the speed was 2000.9 r/min, and the sampling frequency was 12000 Hz. The conditions for sampling are shown in Table 5. Take 24,000 points for analysis. After calculation, the failure characteristic frequency of the bearing outer ring is 101.6 Hz.

Figure 15 shows the time domain diagram and spectrum diagram of the original signal. In Figure 15(a), there is no obvious periodic shock and the signal is noisy. In Figure 15(b), there is no obvious side band phenomenon in the whole spectrum, from which no useful information can be found.

Figures 16 and 17 are the results of processing the experimental signals by using mode FIR and mode STFT, respectively. It can be found from Figure 16 that the frequency band found by this method is too wide to obtain effective information. Comparing Figure 17(a) with Figure 16(a), it is found that the frequency band found by STFT is significantly narrower than that by the FIR filter, but more effective information than the FIR mode. From Figure 16(b), we can get few useful information. Figure 17(b) shows the results of extracting this component and applying Hilbert transformation to obtain the envelope, from which the characteristic frequency and its double frequency can be found, the amplitude of the characteristic frequency is only 0.12, and the double frequency is only 0.07, while the triple frequency cannot be obviously observed due to the noise.

The proposed method is used to process the signal, and the final result is shown in Figure 18. It can be found from the comparison between Figures 17(a) and 18(a) that the frequency band obtained by the new method is (2308 Hz, 3098 Hz), wider than that obtained by mode STFT. In Figure 18(b), it can be clearly seen that the characteristic frequency 102 Hz and 2-3 frequency doubling amplitude are all higher than the amplitude of the surrounding noise components; furthermore, the minimum value is about 0.152 compared to 0.07 in Figure 17(b). This indicates the new method can obtain more

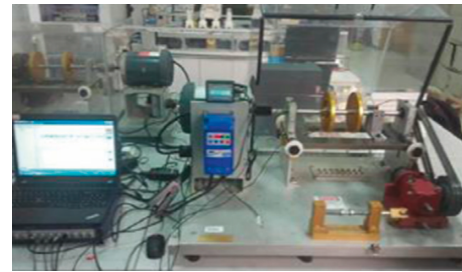


FIGURE 14: Bearing fault test rig.

effective information than the FK method, and the boundary division is more reasonable and has better diagnostic effect.

5.2. Analysis of Bearing Inner Ring Fault Data. The failure data of bearing inner ring were collected in the laboratory of Beijing university of technology by the failure test bench as shown in Figure 19. The rolling bearing type 6307 was adopted. The motor speed was 1496 r/min during measurement, and the sampling frequency was 15360 Hz. 8192 points were taken for analysis. After calculation, it can be obtained that the failure characteristic frequency of the bearing inner ring is 122 Hz. Tables 6 and 7 show the parameters of fault bearing and conditions for sampling.

Figure 20 shows the time domain and spectrum of the original signal. In the time domain diagram, the periodic impact components can be observed. But, the specific fault information cannot be extracted according to the spectrum, due to the presence of noise, and the spectral line in the spectrum diagram is too dense.

Similarly, the two methods of FK are used to process the signal, and the results are shown in Figure 21, where (a) and (b) are the result of using the FIR filter, and (c) and (d) are the result of using STFT. By comparing Figures 21(a) and 21(c), it can be seen that the two methods have overlapping ranges in kurtosis figure. The result of STFT method is a part of the FIR filter method to find the final frequency band result range. However, only characteristic frequency of 122 Hz was observed in the envelope spectrum obtained by the two methods in Figures 21(b) and 21(d). In conclusion, the selected frequency band by FK contains less fault information.

TABLE 4: Parameters of the outer ring fault bearing.

Fault characteristic frequency	Ball diameter	Pitch diameter	Number of ball
101.6 Hz	0.3125 in	1.318 in	8

TABLE 5: Sampling conditions.

Sensor position	Sampling frequency	Sampling points	Motor Speed (r/min)
Motor end	12000 Hz	24000	2000.9

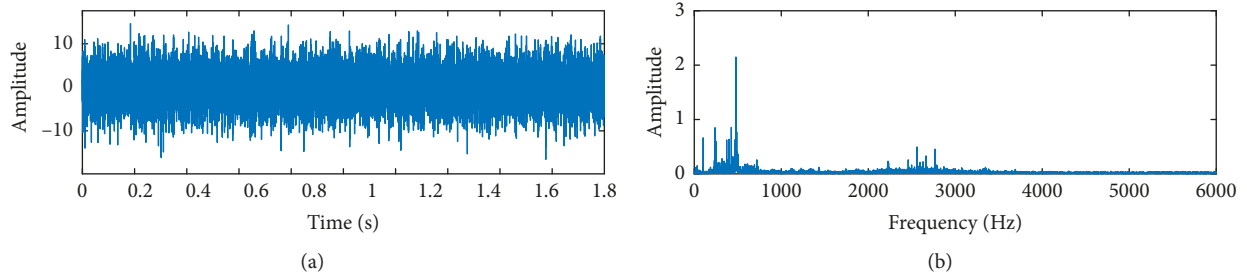


FIGURE 15: (a) Original signal; (b) frequency spectrum.

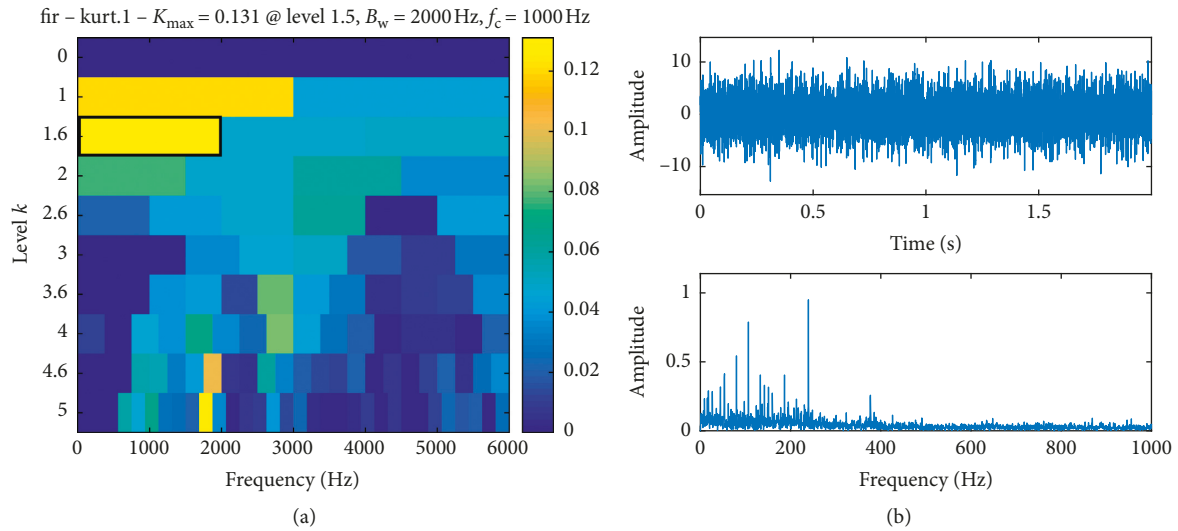


FIGURE 16: (a) Fast kurtogram based on FIR; (b) signal component and its envelope sequence.

To further illustrate the advantages of the proposed method, Figure 22 shows the results by the proposed method. In Figure 22(a), the corresponding frequency band of the maximum kurtosis component is (3081 Hz, 4093 Hz), and the bandwidth is 1015 Hz. The characteristic frequency 102 Hz and its 2–6 frequency doubling are observed in the envelope spectrum (Figure 22(b)). In brief, the inner ring of the bearing has faults, and the new method has obvious advantages compared with FK.

6. Further Verification Based on the Experimental Data of CWRU

The accuracy of the proposed method is further verified by using 48 groups of the bearing inner and outer ring failure

data published by Case Western Reserve University. The experimental data are obtained by artificially manufacturing damage to different parts.

6.1. Further Verification of Outer Ring Fault Data. Outer ring data were selected from “Drive End Bearing Fault Data (fault diameter: 0.007in,)” and the data sampling frequency of this group is $F_S = 12000$ Hz. The bearing type is 6205-2RS deep groove ball rolling bearing. Outer ring fault frequency is $f = 3.5848 \times$ running speed (in Hz). The specific parameters of this bearing are as given in Table 8.

Based on any difference of the following conditions: motor speed, fault position, and sensor position, we selected and obtained 24 groups of outer ring fault signals (number of

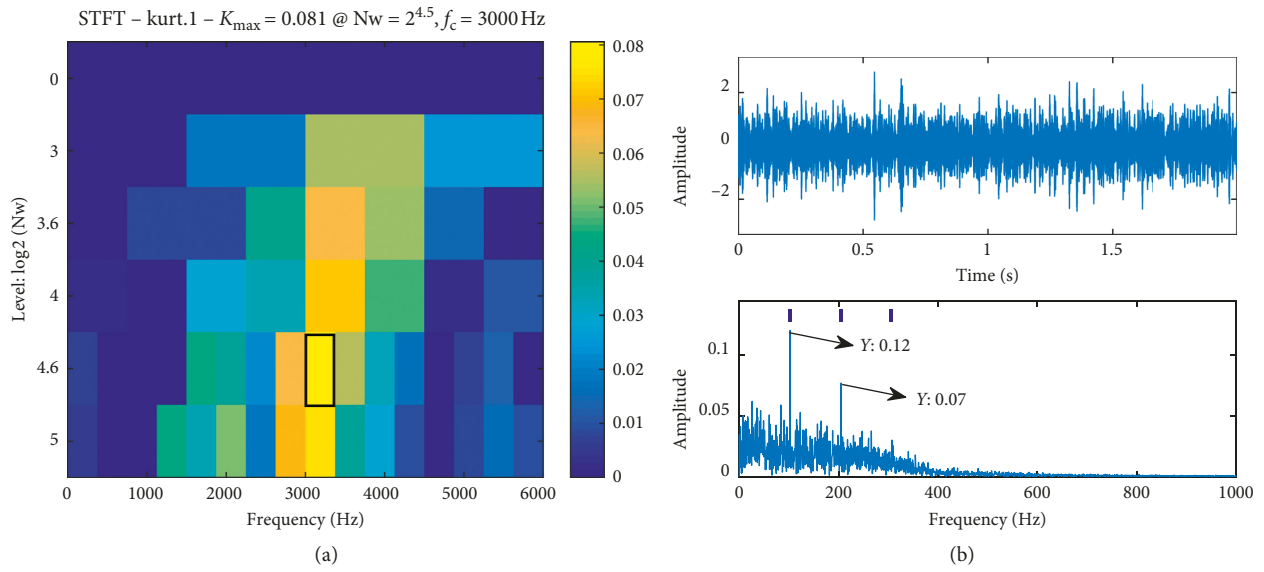


FIGURE 17: (a) Fast kurtogram based on STFT; (b) signal component and its envelope sequence.

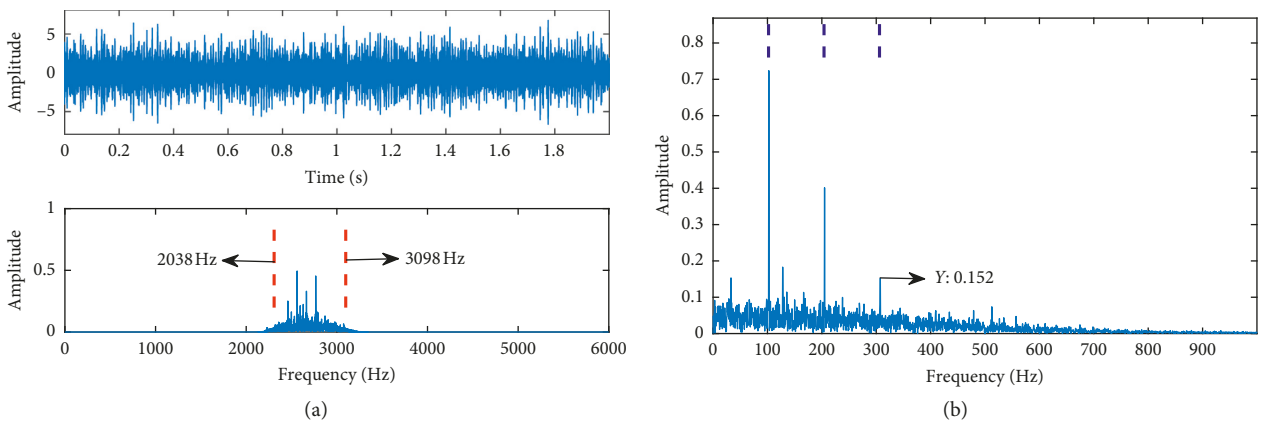


FIGURE 18: (a) Time-domain waveform diagram of the signal component with the maximum kurtosis found by the new method and its frequency band and (b) its envelope sequence.

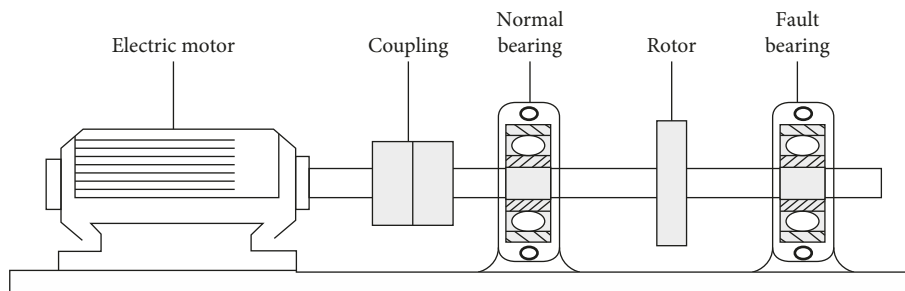


FIGURE 19: Bearing fault test rig.

TABLE 6: Parameters of the inner ring fault bearing.

Fault characteristic frequency	Ball diameter	Pitch diameter	Number of ball
122 Hz	0.5313 in	2.286 in	8

TABLE 7: Sampling conditions.

Sensor position	Sampling frequency	Sampling points	Motor Speed (r/min)
Shaft end	15360 Hz	8192	2000.9

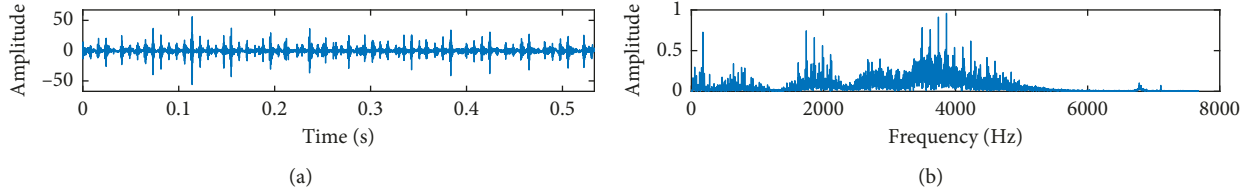


FIGURE 20: (a) Original signal; (b) frequency spectrum.

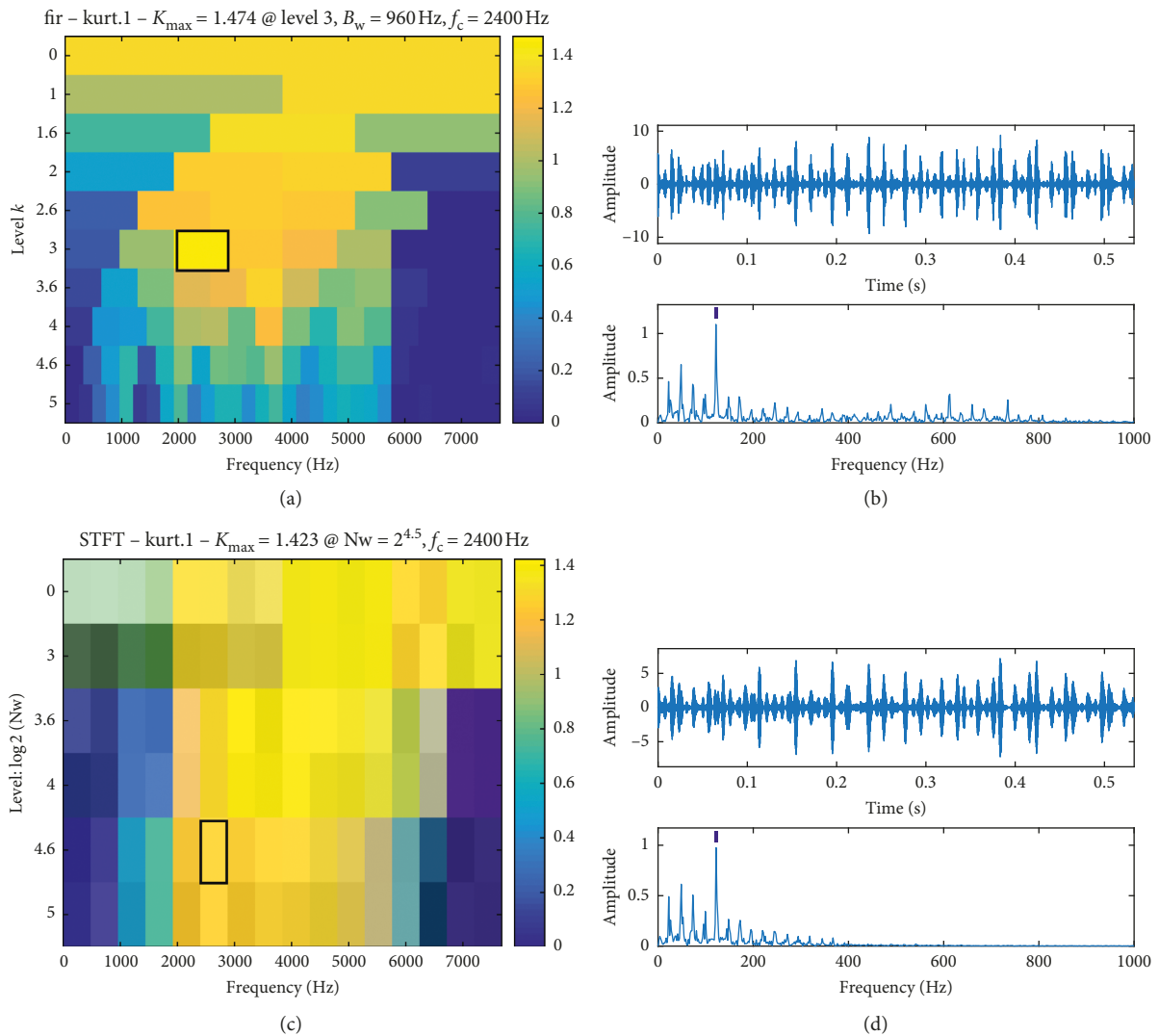


FIGURE 21: (a) Fast kurtogram based on FIR; (b) signal component and its envelope sequence; (c) fast kurtogram based on STFT; (d) signal component and its envelope sequence.

signal points per group, $N = 12000$). The conditions of the selected outer ring fault signals acquisition are shown in Table 9.

We used MOD-EWT, FK-FIR, and FK-STFT to deal with the above data, respectively. Figure 23(a) shows the number of groups that has diagnostic capability (envelope spectrum

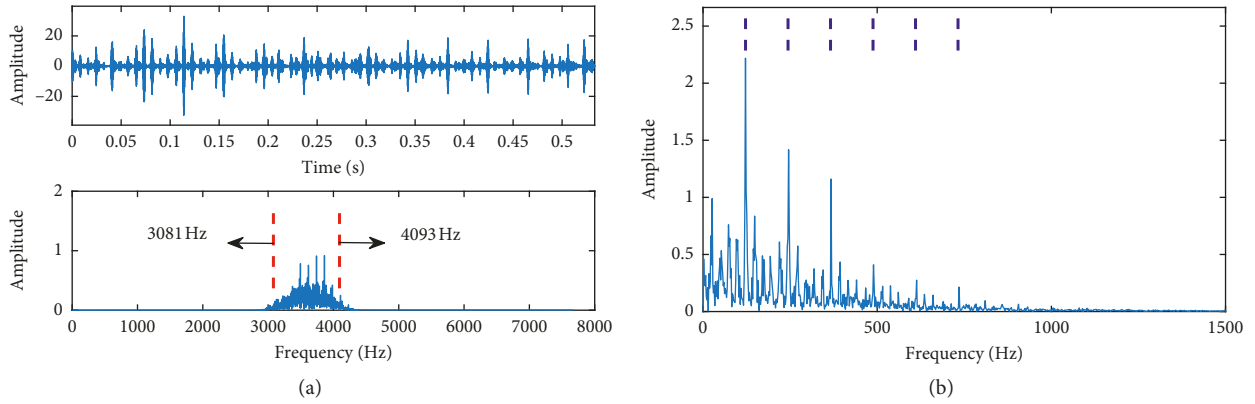


FIGURE 22: (a) Time-domain waveform diagram of the signal component with the maximum kurtosis found by the new method and its frequency band and (b) its envelope sequence.

TABLE 8: Parameters of the bearing.

Type	Inside diameter	Outside diameter	Ball diameter	Pitch diameter
6205-2RS	0.9843 in	2.0472 in	0.3126 in	1.537 in

TABLE 9: Different conditions statement of 24 groups data.

Motor Speed (rpm/min)	Fault position	Sensor position
1797	Centered to loading area	Drive end
1772	Orthogonal to loading area	Fan end
1750		Base
1730		

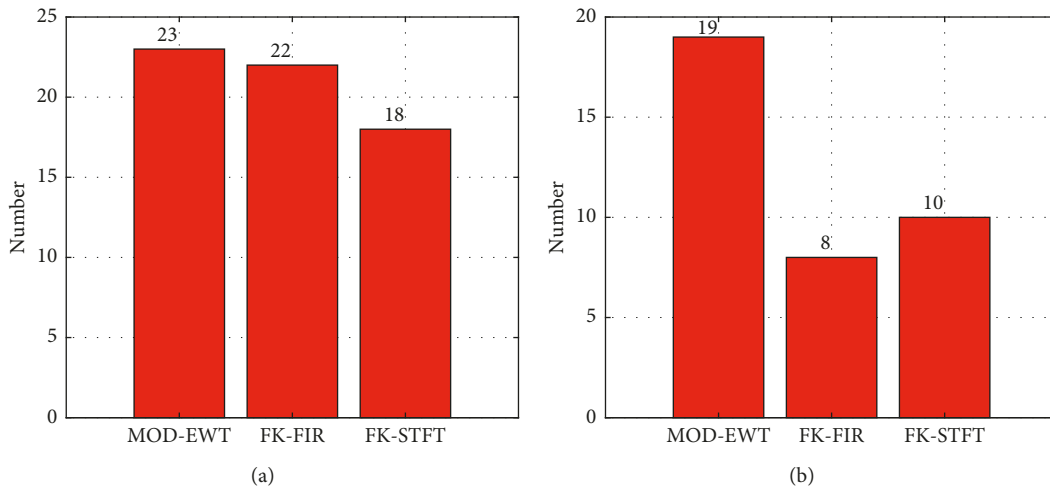


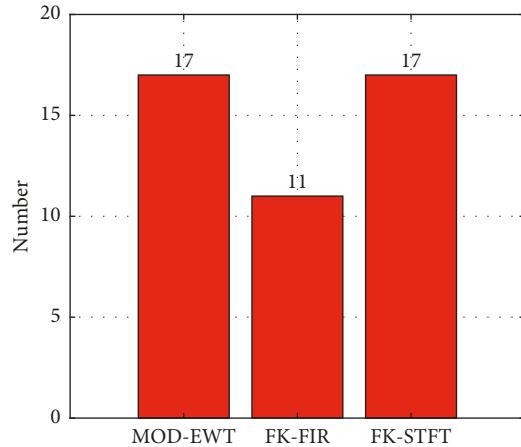
FIGURE 23: Number of groups with (a) diagnostic capability by using the results of three methods and (b) better diagnostic capability by using the results of three methods.

TABLE 10: Parameters of the bearing.

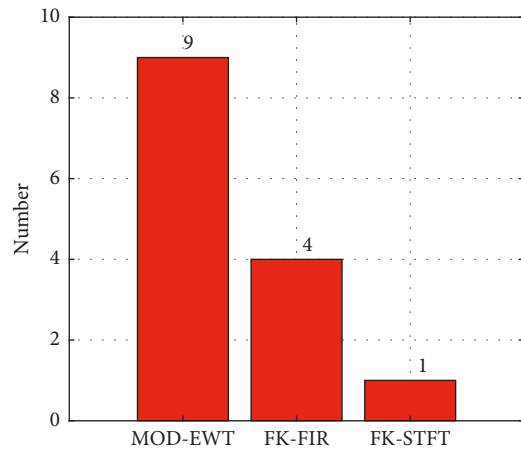
Type	Inside diameter	Outside diameter	Ball diameter	Pitch diameter
6205-2RS	0.6693 in	1.5748 in	0.2656 in	1.122 in

TABLE 11: Different conditions statement of 24 groups data.

Fault diameter	Motor speed (rpm/min)	Sensor position
0.007	1797	Drive end
0.021 in	1772	Fan end
	1750	Base
	1730	



(a)



(b)

FIGURE 24: Number of groups with (a) diagnostic capability by using the results of three methods and (b) better diagnostic capability by using the results of three methods.

shows fault characteristic frequency clearly or 1-2 times of fault characteristic frequency) by using the results of three methods. Figure 23(b) shows the number of groups that has better diagnostic capability (envelope spectrum shows 1-3 times of fault characteristic frequency clearly or 1-4 times or 1-5 times) by using the results of three methods.

As can be seen from Figure 23(a), the three methods do a good job in the diagnosis of the signals, of which MOD-EWT has the highest number of diagnostic groups. In Figure 23(b), the number of MOD-EWT with better diagnostic ability is significantly higher than that of the FK method, which is almost twice of the FK method, and the number of groups with better diagnostic ability accounts for

83% of the total number of diagnostic ability groups. Its accuracy is better reflected.

6.2. Further Verification of Inner Ring Fault Data. The inner ring data were selected from “Fan End Bearing Fault Data (fault diameter: 0.007 in and 0.021 in).” The data sampling frequency of this group is $F_s = 12000$ Hz, and the bearing type is 6203-2RS deep groove ball rolling bearing. The inner ring fault frequency is $f = 4.9469 \times \text{running speed}$ (In Hz). The specific parameters of this bearing are as given in Table 10.

Based on any difference of the following conditions, fault diameter, motor speed, and sensor position, we selected and obtained 24 groups of outer ring fault signals (number of signal points per group, $N = 12000$). The conditions of the selected inner ring fault signals are shown in Table 11.

In the same way as dealing with the inner ring data, the histograms of the three methods are obtained as given in Figure 24.

Due to the complexity of the inner ring fault signal and the influence of noise, the inner ring diagnostic effect is generally lower than that of the outer ring. Figure 24(a) shows that MOD-EWT and FK-STFT have the highest number of diagnostic groups; there are only 11 groups by FK-FIR. This method is too much affected by noise, and the diagnosis is not good. However, in Figure 24(b), FK-STFT has only 1 group with better diagnostic results, while MOD-EWT has nine groups with better diagnostic results. From the results above, we can find the accuracy of the proposed method is better than that of the FK methods.

7. Conclusion

In this paper, a novel bearing fault diagnosis method is proposed, which uses EWT for filtering. The proposed algorithm of frequency band multidivisional and overlapped (MDO-EWT) is to replace the FK bisection method. By verification of simulated signals, it is shown that the proposed method can correctly find the signal with center frequency as $f = 1/2^n \times F_s$ and reasonable bandwidth; the energy ratio is used to prove the accuracy of the proposed method. With the analysis and verification of the experimental data, it is shown that the proposed method has a better performance than FK on extracting the maximum kurtosis component from bearing outer and inner ring fault signals with noise. Compared with the results obtained by FK, the new method is superior in accuracy and effectiveness.

In the future, we will be committed to the optimization of the algorithm, so that its use can be extended.

Data Availability

The experimental data [.txt] and [.mat] used to support the findings of this study were supplied by the research group of Key Laboratory of Advanced Manufacturing Technology under license and so they cannot be made publicly available, and the requests for access to these data should be made to the corresponding author.

Conflicts of Interest

The authors declare no conflicts of interest related to this manuscript.

Acknowledgments

The authors would like to gratefully acknowledge the National Natural Science Foundation of China (grant nos. 51775005 and 51675009) and the Key Laboratory of Advanced Manufacturing Technology for their support. Finally, the authors would like to appreciate anonymous reviewers and editors for their valuable comments and constructive suggestions. Funding was provided by the National Natural Science Foundation of China (grant nos. 51775005 and 51675009).

References

- [1] L. Cui, J. Huang, and F. Zhang, "Quantitative and localization diagnosis of a defective ball bearing based on vertical-horizontal synchronization signal analysis," *IEEE Transactions on Industrial Electronics*, vol. 64, no. 11, pp. 8695–8706, 2017.
- [2] Y. Xu, W. Tian, K. Zhang, and C. Ma, "Application of an enhanced fast kurtogram based on empirical wavelet transform for bearing fault diagnosis," *Measurement Science and Technology*, vol. 30, no. 3, article 035001, 2019.
- [3] R. Dwyer, "Use of the kurtosis statistic in the frequency domain as an aid in detecting random signals," *IEEE Journal of Oceanic Engineering*, vol. 9, no. 2, pp. 85–92, 1984.
- [4] V. Capdevielle, C. Serviere, and J. L. Lacoume, "Blind separation of wide-band sources: application to rotating machine signals," in *Proceedings of the 8th European Signal Processing Conference (EUSIPCO 1996)*, pp. 1–4, IEEE, Trieste, Italy, September 1996.
- [5] D. He, X. Wang, S. Li, J. Lin, and M. Zhao, "Identification of multiple faults in rotating machinery based on minimum entropy deconvolution combined with spectral kurtosis," *Mechanical Systems and Signal Processing*, vol. 81, pp. 235–249, 2016.
- [6] J. Li, Y. Zhong, and H. Gao, "Rolling element bearing fault detection using PPCA and spectral kurtosis," *Measurement*, vol. 75, pp. 180–191, 2015.
- [7] F. Combet and L. Gelman, "Optimal filtering of gear signals for early damage detection based on the spectral kurtosis," *Mechanical Systems and Signal Processing*, vol. 23, no. 3, pp. 652–668, 2009.
- [8] N. Sawalhi, R. B. Randall, and H. Endo, "The enhancement of fault detection and diagnosis in rolling element bearings using minimum entropy deconvolution combined with spectral kurtosis," *Mechanical Systems and Signal Processing*, vol. 21, no. 6, pp. 2616–2633, 2007.
- [9] J. Antoni, "The spectral kurtosis: a useful tool for characterising non-stationary signals," *Mechanical Systems and Signal Processing*, vol. 20, no. 2, pp. 282–307, 2006.
- [10] J. Antoni and R. B. Randall, "The spectral kurtosis: application to the vibratory surveillance and diagnostics of rotating machines," *Mechanical Systems and Signal Processing*, vol. 20, no. 2, pp. 308–331, 2006.
- [11] J. Antoni, "Fast computation of the kurtogram for the detection of transient faults," *Mechanical Systems and Signal Processing*, vol. 21, no. 1, pp. 108–124, 2007.
- [12] J. Obuchowski, A. Wyłomańska, and R. Zimroz, "Selection of informative frequency band in local damage detection in rotating machinery," *Mechanical Systems and Signal Processing*, vol. 48, no. 1-2, pp. 138–152, 2014.
- [13] Y. Lei, J. Lin, Z. He, and Y. Zi, "Application of an improved kurtogram method for fault diagnosis of rolling element bearings," *Mechanical Systems and Signal Processing*, vol. 25, no. 5, pp. 1738–1749, 2011.
- [14] X. Wang, Z. He, and Y. Zi, "Spectral kurtosis of multiwavelet for fault diagnosis of rolling bearing," *Journal of Xi'an Jiaotong University*, vol. 44, no. 3, pp. 77–81, 2010.
- [15] F.-Q. Tian, R. Luo, W. Li, and Y. Xie, "Improved harmonic wavelet packet kurtogram and its application," *Journal of Shanghai Jiaotong University*, vol. 48, no. 1, pp. 39–44, 2014.
- [16] C. Li, D. Cabrera, J. V. de Oliveira, R.-V. Sanchez, M. Cerrada, and G. Zurita, "Extracting repetitive transients for rotating machinery diagnosis using multiscale clustered grey info-gram," *Mechanical Systems and Signal Processing*, vol. 76-77, pp. 157–173, 2016.
- [17] S. Dai, Y. Guo, X. Wu et al., "Improvement on fast kurtogram algorithm based on sub-frequency-ban spectral kurtosis average," *Journal of Vibration and Shock*, vol. 34, no. 7, pp. 98–102, 2015.
- [18] X. Zhang, J. Kang, L. Xiao, J. Zhao, and H. Teng, "A new improved kurtogram and its application to bearing fault diagnosis," *Shock and Vibration*, vol. 2015, Article ID 385412, 22 pages, 2015.
- [19] J. Gilles, "Empirical wavelet transform," *IEEE Transactions on Signal Processing*, vol. 61, no. 16, pp. 3999–4010, 2013.
- [20] M. Kedadouché, M. Thomas, and A. Tahan, "A comparative study between empirical wavelet transforms and empirical mode decomposition methods: application to bearing defect diagnosis," *Mechanical Systems and Signal Processing*, vol. 81, pp. 88–107, 2016.
- [21] J. Gilles and K. Heal, "A parameterless scale-space approach to find meaningful modes in histograms—application to image and spectrum segmentation," *International Journal of Wavelets, Multiresolution and Information Processing*, vol. 12, no. 6, article 1450044, 2014.
- [22] Y. Xu, K. Zhang, C. Ma, X. Li, and J. Zhang, "An improved empirical wavelet transform and its applications in rolling bearing fault diagnosis," *Applied Sciences*, vol. 8, no. 12, article 2352, 2018.

